Comparative dynamic analysis of two-rotor wind turbine on spar-type, semi-submersible, and tension-leg floating platforms

Omar El Beshbichi [*], Yihan Xing, Muk Chen Ong

Department of Mechanical and Structural Engineering and Materials Science, University of Stavanger, Stavanger, Norway

A R T I C L E   I N F O

A B S T R A C T

Multi-rotor floating offshore wind turbines have been recently proposed as an innovative technology to further reduce the cost of offshore wind energy. Even though examples of commercial prototypes are present, the literature lacks studies on the dynamic performance of such systems. This work presents a comparative analysis of a two-rotor wind turbine concept mounted on spar-type, semi-submersible, and tension-leg platforms. Their short-term performance is assessed by considering six different load cases considering directionally congruent turbulent wind profiles and irregular sea states. The analysis is carried out through an in-house fully-coupled code developed in Modelica. AeroDyn v15 within FAST v8 by NREL is coupled to the Modelica code to achieve blade-element momentum capabilities. Results indicate that platform yaw motion is an important dynamic mode of the systems, particularly for the spar configuration. Stiffer station-keeping lines and longer fairlead distance to the platform centerline reduce significantly yaw motion, as in the case of the semi-submersible and tension-leg configurations. Large tower base bending moment standard deviations and the associated concentration of energy at the platform heave and pitch motion frequencies indicate an increased risk for fatigue damage for the TLP configuration, especially at above-rated wind speeds. Moreover, large tendon loads can pose concerns in terms of fatigue and limit state performance. Large mean platform pitch angle and yaw standard deviation contribute to the reduction of electric power output quality. Extreme storm conditions greatly increase the response standard deviation, especially for the semi-submersible configuration.

1. Introduction

The offshore wind industry has been experiencing significant expansion in the last decade, achieving in 2020 a total offshore wind capacity of about 6.1 GW (Global Wind Energy Council, 2022). Many are the advantages of employing wind turbines in the offshore environment. First, the wind speed is much greater and steadier than in inland environments. Moreover, offshore deployment allows for less intrusive interactions with populated areas. Most of the current wind energy exploitation is located in shallow waters, where bottom-fixed foundations are economically feasible. Floating offshore wind turbines (FOWTs) have been recently proposed as technological means to achieve wind energy deployment in offshore areas with significant water depth (exceeding the conventional limit of 50 m) without increasing the associated levelized cost of energy (LCoE) (Cruz and Atcheson, 2016). Hywind Scotland was the first FOWT farm to be commercially commissioned in 2017 by Equinor ASA off the coast of Peterhead, Scotland (Equinor, 2022). The farm is composed of five spar-type FOWTs of about 6 MW. More recently, many other commercial projects have been commissioned. Notable examples are the European

projects initiated by Principle Power, where semi-submersible floating platforms are used (Principle Power, 2022).

Another means of reducing the LCoE of offshore wind energy is by means of multi-rotor floating configurations. Multi-rotor wind turbines have been put forward for the reduction of costs associated with exceptionally big wind turbine components, chiefly blades. The blade mass increases at a higher rate than the associated increase in net energy output (Jamieson and Branney, 2012). Scaling big wind turbines in an array of smaller wind turbines thus allows for a net reduction of the rotor mass employed and the associated final cost. Moreover, employing multiple wind turbines on the same floating platform leads to significant advantages such as, for instance, the reduction of costs associated with the manufacturing and sharing of platform and station-keeping systems, fewer installations, and cheaper offshore operations dealing with smaller mechanical components.

Vestas A/S deployed a four-rotor wind turbine 225 kW each (4R-V29) at the Technical University of Denmark from 2016 to 2019, demonstrating faster wake recovery and marginally higher power production if compared to an analogous single-rotor configuration (van der

Laan et al., 2019). Notable examples of multi-rotor FOWT systems under development are TwinWay by Hexicon (2021a) and Flex2Power by Rosenberg Worley AS (Flex2Power, 2022). The first is a two-rotor wind turbine mounted on a semi-submersible platform. A TwinWay demonstrator is planned to be deployed in 2022 at the MetCentre area in Norway (Hexicon, 2021b). The second instance is a modularized platform for combined wind, wave, and solar energy production. Other conceptual examples are Wind Catching by Wind Catching Systems (WCS) (Wind Catching Systems, 2022) and Nezzy[2], under development by EnBW and Aerodyn Engineering (EnBW, 2021b; Aerodyn Engineering, 2021). The former is composed of a steel grid of 117 small turbines mounted on a semi-submersible floating platform, while the latter is composed of a two-rotor wind turbine supported by a light Y-shaped semi-submersible platform (EnBW, 2021a).

To date, the literature lacks a thorough depiction of the dynamic performance of multi-rotor FOWTs. Previous work presented a novel object-oriented approach to model the fully-coupled dynamics of FOWTs, aiming at the dynamic analysis of multi-rotor concepts (El Beshbichi et al., 2021b). The method was then employed to study the dynamics of a two-rotor wind turbine concept mounted on a spar-type floating platform (El Beshbichi et al., 2021a). Results showed significant platform yaw motion, associated with turbulence intensity and related with the thrust distribution on the structure. It was also shown how platform yaw motion can be mitigated by properly adjusting the rotor-collective blade-pitch control strategy.

In this work, the dynamic analysis of a two-rotor wind turbine concept (2WT) mounted on spar-type, semi-submersible, and tension-leg (TLP) platforms is performed. The 2WT concept makes use of baseline NREL 5-MW wind turbines and a tower structure as proposed in El Beshbichi et al. (2021a). The spar and TLP platforms considered are preliminary designs defined by means of simplified hydrostatic considerations, while the semi-submersible platform design is based upon the well-known OO-Star design (Berthelsen, 2015).

Currently available commercial and open-source fully-coupled tools for the dynamic analysis of floating wind turbines are not able to accommodate multi-rotor systems with the flexibility and performance needed for conceptual analysis. To address this gap, a novel tool has been developed which offers easy implementation of arbitrary floating platforms and number of turbines employed. The tool is developed in Modelica v3.2.3 through the open-source platform OpenModelica v1.16.2 and is based on the freely-available Modelica Standard Library (MSL) (The Modelica Association, 2017; OSMC, 2021). Modelica is a non-proprietary, object-oriented, equation-based language used for the convenient dynamic modeling of complex multi-domain systems. The tool implements industry-standard fidelity levels, and a benchmarking exercise of the code against FAST v8 showed an accurate response and good numerical performance. The blade-element momentum (BEM) package within FAST v8, i.e., AeroDyn v15, has been coupled to the Modelica code because of its widespread use in academic research (Jonkman and Buhl, 2005; Moriarty and Hansen, 2005). More complex aerodynamic effects, such as the aerodynamic interaction between rotors, are not considered to date. AeroDyn v15 is well-suited to be further modified, as it would be needed in future work for the implementation of a correction factor accounting for aerodynamic interactions between rotors within the BEM formulation. The tool will be released open-source in the next future. The structural code relies upon the multi-body systems (MBS) package within the MSL. Tower and blades are assumed rigid in this study.

A series of load cases (LCs) are used to assess the dynamic performance of the three FOWT concepts. Performance parameters, such as global rigid motions, tower base bending moment, and upstream mooring line tension are compared. This type of comparison is able to highlight important dynamic differences of the floating systems undergoing the same hydrodynamic and aerodynamic loads.

Table 1
NREL 5-MW baseline wind turbine specifications (Jonkman, 2007).

Rated power	MW	5
Rotor orientation, configuration		Upwind, 3 blades
Control		Variable speed, collective pitch
Drivetrain		High speed, multiple-stage gearbox
Rotor, hub diameter	m	126, 3
Rated tip speed	m/s	80
Hub height	m	90
Rotor mass	kg	110×10^3
Nacelle mass	kg	240×10^3
Cut-in, rated, cut-out wind speed	m/s	3, 11.4, 25
Cut-in, rated rotor speed	rpm	6.9, 12.1

2. Two-rotor wind turbine design

The 2WT structure employed corresponds to the design proposed in El Beshbichi et al. (2021a). The structure is composed of a primary vertical tapered tower, two horizontal tapered arms, and an additional vertical cylinder as depicted in Fig. 1. Wires are employed to distribute static bending loads as compression loads on the primary tower. The primary tower base outer diameter is about 6.28 m (thickness of about 0.03 m), while its top outer diameter is about 4.79 m (thickness of about 0.0215 m). A simplified structural design preventing yield is employed considering the RNAs weight acting at the hubs, the horizontal arms self-weight, and the maximum environmental loading acting on the structure, i.e., maximum aerodynamic thrust at the hubs. A safety factor of 1.4 is also employed to obtain a conservative design. Further information about tower structural dimensioning and inertial specifications can be found in El Beshbichi et al. (2021a). More sophisticated considerations, such as fatigue, buckling, and inertial amplification effects, are not accounted to date. Nonetheless, a more detailed structural design may be defined in future work. Two standard NREL 5-MW wind turbines are also employed in the 2WT design (Jonkman, 2007). The space between rotors is set to 10% of the rotor radius, similarly to the multi-rotor concept by Vestas A/S installed at DTU (Bastankhah and Abkar, 2019). Major wind turbine specifications are listed in Table 1.

3. Floating platform designs

Three floating platform configurations are considered for this study, i.e., a spar-type, a semi-submersible, and a TLP, as depicted in Fig. 2. The spar and TLP platforms are early designs that have been specified for use with the 2WT configuration under consideration. On the other hand, the semi-submersible design is the OO-Star Wind Floater Semi 10-MW (for brevity, OO-Star) (Berthelsen, 2015). This design has been proposed within the second stage of the EU-funded LIFES50+ project (LIFES50+, 2022). The OO-Star design is also originally intended to be employed with the DTU 10-MW reference wind turbine (Bak et al., 2013).

The spar platform design is equal to the one proposed in El Beshbichi et al. (2021a). The structure is made of steel. Hydrostatic considerations are used to select an optimal spar geometry. The design criteria are (1) the enforcement of hydrostatic equilibrium of the full-system affected by mooring lines by properly adjusting the ballast mass, (2) the limitation of the static pitch angle to about 5 deg under maximum external loading, (3) the enforcement of pitch and heave natural periods larger than about 25–30 s in order to avoid first-order wave effects, and (4) the utilization of as little mass as possible. A complete account of the spar design can be found in El Beshbichi et al. (2021a) where platform design spaces are employed to determine the optimal configuration. Geometrical parameters relative to the specified spar platform configuration are listed in Table 2. The configuration employs three catenary mooring lines with a length of about 900 m, a diameter of 0.09 m, and an equivalent mass density of 200 kg/m. The lines are mounted at 120 deg from each other, starting from the
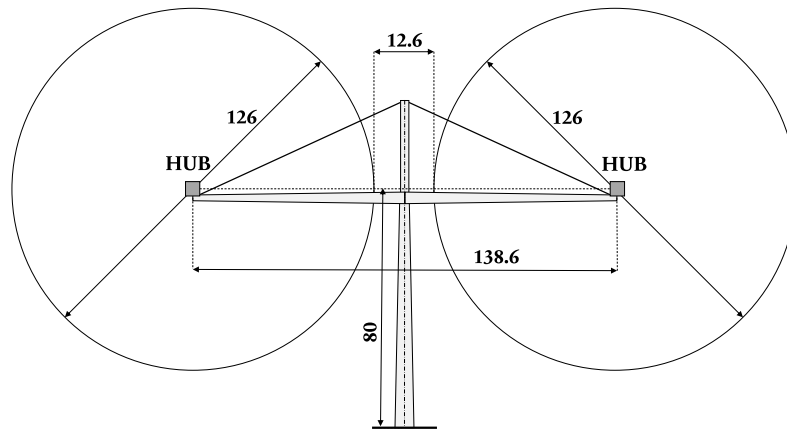
Fig. 1. Multi-rotor wind turbine geometry [m] (El Beshbichi et al., 2021a).
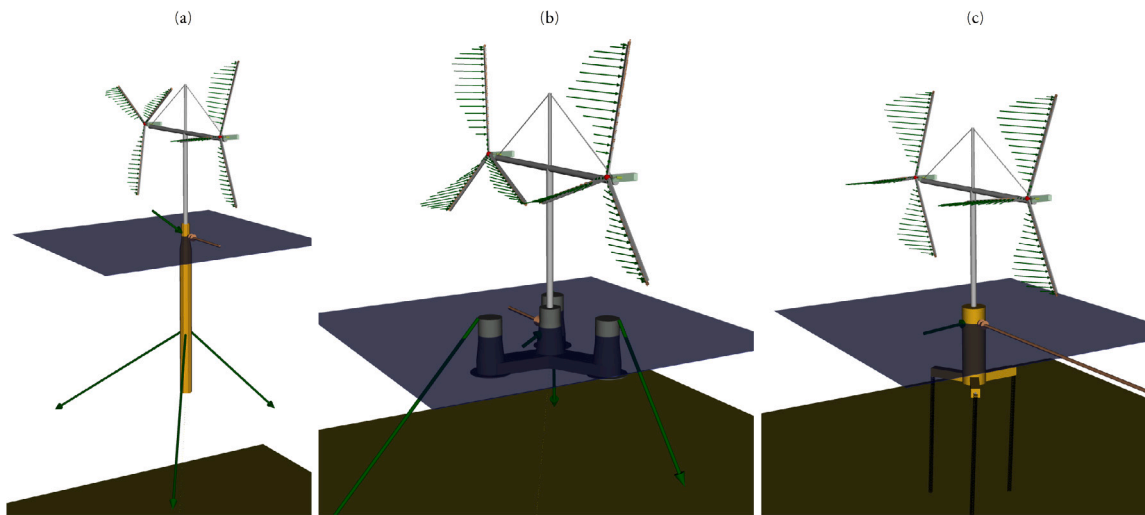

Fig. 2. Multi-rotor floating wind turbine configurations selected in the present study. (a) Spar-type platform. (b) Semi-submersible platform (OO-Star design Berthelsen, 2015). (c) TLP platform.

Table 2
Spar platform configuration selected (El Beshbichi et al., 2021a).

Draft	m	140
Diameter (tapered at SWL)	m	10.5 (7.5)
Fairlead distance from SWL	m	86.5
Fairlead radius	m	5.78
Freeboard to tower base	m	10

Table 3
TLP platform configuration selected.

Number of pontoons	–	3
Draft	m	43
Main hull diameter	m	16
Hull height	m	53
Pontoon length to axis	m	32.5
Pontoon square cross-section height	m	6
Pontoon vertical location from the SWL	m	40
Tendon outer diameter	m	1.3
Freeboard to tower base	m	10

downwind direction. The spar configuration is employed at a water depth of about 320 m.

The TLP platform design is carried out following preliminary considerations from Bachynski and Moan (2012). The design employs a main cylindrical hull and three rectangular pontoons supporting the tension legs. The structure is made of steel. The pontoons are mounted at the cylinder base and are displaced 120 deg from each other, starting from the downwind direction. A square pontoon cross-section is also assumed. Design is based on hydrostatic considerations. The design criteria used are (1) the enforcement of surge and sway natural periods longer than 25 s to avoid first-order wave excitation, (2) the enforcement of heave, roll, and pitch natural periods shorter than 3.5 s to avoid first-order wave excitation, (3) the limitation of the mean offset to about 5% of the water depth under maximum aerodynamic loading and hydrodynamic loading, (4) the yield assessment of the tendons with a safety factor (SF) equal to 2, and (5) the enforcement of a displaced volume higher than 2000 m³ for increased stability under extreme

environmental conditions. Major platform and tendon parameters are adjusted heuristically until a feasible configuration fulfilling all design constraints is obtained. Surge and pitch natural periods are computed by considering hydrodynamic coupling. Hydrodynamic loading for off-set estimation accounts for a sea state with a significant wave height of 4 m and a period of 10 s. Geometrical parameters relative to the specified TLP platform configuration are listed in Table 3. The TLP configuration is employed at a water depth of about 130 m.

The description of the OO-Star platform design is public (Berthelsen, 2015; Pegalajar-Jurado et al., 2018). The platform is made up of a star-shaped pontoon connecting the central tapered column with the three outer tapered columns. The pontoons are displaced 120 deg from each other, starting from the upwind direction. The structure is made of
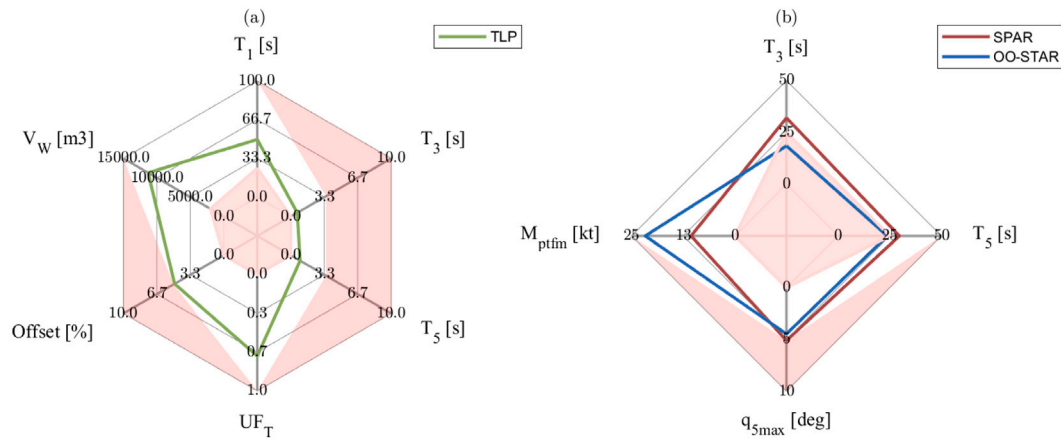
Fig. 3. Design criteria used in preliminary platform design. Values outside of the optimal design range are within the red-graded area. (a) TLP design criteria (Bachynski and Moan, 2012). (b) spar design criteria (OO-Star performance when employed with 2WT prototype is also included) (El Beshbichi et al., 2021a). (For interpretation of the references to color in this figure legend, the reader is referred to the web version of this article.)

Table 4
OO-Star platform main geometrical parameters (Berthelsen, 2015).

Draft	m	22
Pontoon length to axis	m	37
Pontoon height	m	6.5
Pontoon width	m	17
Outer column height (from pontoon)	m	24.5
Central column height (from pontoon)	m	26
Central column diameter (tapered)	m	16.2 (12.05)
Outer column diameter (tapered)	m	15.8 (13.4)
Fairlead radius	m	44
Fairlead distance from SWL	m	−9.5
Freeboard to tower base	m	11

concrete. The main geometrical parameters of the platform are listed in Table 4. The configuration employs three catenary mooring lines with a length of about 703 m, a diameter of 0.137 m, and an equivalent mass density of about 375 kg/m. The lines are mounted at 120 deg from each other, starting from the upwind direction. Moreover, the original mooring system employs clumped masses, mounted at 118 m from the fairlead along the mooring lines, in order to achieve greater pre-tension per unit length. In this work, the clump mass is removed and equivalence is achieved by increasing the mooring line mass per unit length to get the same static fairlead tension. An equivalent mass density of 650 kg/m is thus obtained. The ballast mass has been also properly adjusted for utilization with the 2WT system. Additional ballasting of about 688 tonnes is included to achieve equivalent draft and water displacement. The OO-Star configuration is employed at a water depth of about 130 m.

Fig. 3 gives a graphical representation of the design criteria used in preliminary platform design and the corresponding design performance. Red grading is used to highlight values outside the optimal design range. The figure shows both the TLP design parameters (a) and the spar design parameters (b). The OO-Star performance when employed together with the 2WT prototype is also included (b). To be noted the low heave period for the OO-Star configuration (about 18.5 s), which may lead to amplification of platform heave motion under extreme sea states.

Table 5 lists the inertial and hydrostatic properties of each platform. Hydrostatic restoring stiffness values are derived from metacentric height relationships and are referred to the total center of gravity (CoG) of the system (Faltinsen, 1990). The restoring stiffness values can be estimated as:

$$C_{33} = \rho g A_{wp} \tag{1}$$

$$C_{44} = \rho g V_w (z_G - z_B) + \rho g I_{yy} \tag{2}$$

$$C_{55} = \rho g V_w (z_G - z_B) + \rho g I_{xx} \tag{3}$$

where C_{33} is the heave restoring stiffness, C_{44} is the roll restoring stiffness, C_{55} is the pitch restoring stiffness, ρ is the water density, g is the acceleration due to gravity, V_w is the water displacement, A_{wp} is the waterplane area, z_G is the depth to the total CoG, z_B is the depth to the center of buoyancy (CoB), I_{yy} is the roll waterplane second moment of area, and I_{xx} is the pitch waterplane second moment of area. This formulation assumes positive depths from the SWL. These formulations can be used as indicators for the stability of the unmoored floating system. The roll and pitch hydrostatic restoring stiffness values associated with the TLP platform are negative given the relatively small waterplane second moment of area and the negative difference between depth to total CoG of the system and depth to CoB. This clearly indicates hydrostatic instability of the TLP system if tendon loads are disregarded. On the other hand, hydrostatic coefficients relative to the spar and OO-Star configurations are positive. This indicates hydrostatic stability of the system even without considering the further stabilizing effect of the catenary system. It is assumed that the OO-Star platform CoG location is not significantly affected by the additional ballast mass employed.

4. Non-linear coupled analysis

The non-linear fully-coupled dynamic responses of the FOWT concepts are obtained by means of an in-house code implemented in the language Modelica (The Modelica Association, 2017). The open-source platform OpenModelica is also employed (OSMC, 2021). The object-oriented coding approach allows for easy implementation of models relative to concepts of arbitrary platform configuration and number of wind turbines. The structural modeling is carried out by using the MBS package within the freely-available MSL (The Modelica Association, 2008). Previous work described the method in some detail, where simplified aerodynamic loads computed by means of steady-state coefficients were employed (El Beshbichi et al., 2021b). More recently, full BEM capabilities have been achieved by integrating into Modelica the well-established code Aerodyn v15 within FAST v8 by NREL (Jonkman and Buhl, 2005; Moriarty and Hansen, 2005). An aerodynamic sub-routine, written in Fortran 90 and compiled as a dynamic link library (DLL), has been developed to call AeroDyn v15 at each time step. The result is a direct functional relationship between the dynamic state of the system and the associated steady-state aerodynamic loads. An aerodynamic subroutine instance is called for each rotor considered in the model. The aerodynamic DLL has been interfaced with the Modelica code by means of a buffer written in C.

Table 5
Platforms inertial and hydrostatic properties.

		SPAR	OO-STAR	TLP
Depth to CoG	m	121.5	15.2	27.9
Depth to CoB	m	72	14.2	25.83
Water displacement, V_w	m^3	1.17×10^4	2.35×10^4	1.13×10^4
Mass (including ballast)	kg	1.06×10^7	2.17×10^7	2.59×10^6
Roll moment of inertia about CoG	kgm^2	1.13×10^{10}	9.43×10^9	5.76×10^8
Pitch moment of inertia about CoG	kgm^2	1.13×10^{10}	9.43×10^9	5.76×10^8
Yaw moment of inertia about centerline	kgm^2	1.7×10^8	1.63×10^{10}	8.02×10^7
Waterplane area, A_{wp}	m^2	45.4	548.9	201
Roll waterplane second moment of area, I_{yy}	m^4	163.8	2.95×10^5	3.22×10^3
Pitch waterplane second moment of area, I_{xx}	m^4	163.8	2.95×10^5	3.22×10^3
Heave hydrostatic restoring stiffness, C_{33}	N/m	4.56×10^5	5.51×10^6	2.02×10^6
Roll hydrostatic restoring stiffness, C_{44}	Nm/rad	3.42×10^9	2.16×10^9	-1.42×10^9
Pitch hydrostatic restoring stiffness, C_{55}	Nm/rad	3.42×10^9	2.16×10^9	-1.42×10^9
Total mass (platform, ballast, tower, nacelle, rotor)	kg	1.18×10^7	2.36×10^7	8.82×10^6
Depth to total CoG (platform, ballast, tower, nacelle, rotor)	m	100.9	10.24	13.01
Distance between total CoG and CoB	m	28.9	−3.42	−12.82

In this work, tower structure and blades are assumed to be rigid. The study of more complex aeroelastic effects is left as a subject for further investigation. The integration method *ida* is used to solve the equations of motion (EoM) of the system. A time interval of 0.1 s is used for time series storage, sufficient to cover rigid dynamics. Different tolerances are selected in a trade-off between simulation time and a sufficient level of accuracy and stability of the solver. It is found that the spar configuration needs a tolerance of at least $1x10^{-5}$ in order to avoid aerodynamic loads scattering. The OO-Star configuration, however, is found to be more stable and a tolerance of 1×10^{-3} is used without issues. A tolerance of about 1×10^{-6} is used instead in the TLP configuration, as lower tolerance levels are harder to solve. The linear solver *totalpivot* is used, as it is found to be the most robust algorithm available in this context. The non-linear solver *kinsol* is also used. The simulation time used is equal to 4000 s, where the first 400 s are removed to discard initial transients. A net 1-h simulation time is thus used to compute the resulting dynamic response parameters.

4.1. Aerodynamic modeling

Aerodynamic loads are computed by means of the BEM formulation. The NREL code InflowWind within FAST is integrated into Modelica to compute the wind velocity components at each aerodynamic node. Global turbulent wind velocity profiles are preventively generated in TurbSim and imported in InflowWind as binary .bts files (Jonkman, 2009). A 15 × 15 grid-point matrix dimension is used. The grid height is 160 m and the grid width is 300 m, large enough to cover both rotors. A time step of 0.05 s is used, and a total usable time series of 4000 s is computed. A steady airfoil aerodynamic model is used in all cases considered. The aerodynamic interaction between the rotors due to their proximity is to date not considered. Previous work in different fields regarding similar systems, such as the study of thrust imbalance due to aerodynamic interactions in Unmanned Aerial Vehicles (UAVs), suggests that the effect of aerodynamic interactions on the aerodynamic loads acting on the system may not be significant enough to compromise the results obtained with the method employed in this work (Zhou et al., 2017; Alvarez and Ning, 2019). At any rate, this effect should later be investigated by means of higher fidelity methods. The tower influence on the local wind velocity profile is also not included, as well as the aerodynamic drag acting on the tower.

4.2. Hydrodynamic modeling

In the simulations presented in this work, the hydrodynamic loads acting on the floating platforms are computed by means of linear wave theory. The commercial software DNV HydroD-Wadam within SESAM is used to solve the potential flow frequency-domain hydrodynamics (DNV, 2021). Loads are computed at the SWL. External

lookup tables are used to store and import in Modelica time realizations of irregular wave loads. A state-space representation is employed to approximate the effect of radiation damping in Modelica (Cummins, 1962). A state-space approximation order equal to two is used. The added mass matrix from radiation is included by computing its value at infinite frequency. Motions of a rigid floater can then be computed by using the associated equations (Jonkman, 2007):

$$[M]\ddot{\underline{q}} + [C]\underline{q} + C_{0,3} = -[A]_{inf}\ddot{\underline{q}} - \int_0^t [K(t-\tau)]\dot{\underline{q}}d\tau + \underline{F}_w + \underline{F}_g \qquad (4)$$

where $\underline{q}$ are the platform degrees of freedom, $[M]$ is the inertia tensor of the system, $[C]$ is the hydrostatic matrix, $C_{0,3}$ is the restoring load, $[A]_{inf}$ is the added mass term from hydrodynamic radiation at infinite wave frequency, $[K(t)]$ is the retardation-kernel matrix from hydrodynamic radiation, $\underline{F}_w$ are the incident wave loads, and $\underline{F}_g$ are the gravitational loads. Further information about hydrodynamic modeling can be found in El Beshbichi et al. (2021b).

Figs. 4, 5, and 6 show, respectively, the major components of the radiative added mass, radiative potential damping, and incident wave loading for each FOWT configuration. Added mass in the platform pitch direction is highest for the spar configuration given the long-drafted geometry. The OO-Star configuration is subjected to the highest radiation damping in all directions. Radiation damping is especially high in the platform heave and yaw directions given the significantly greater waterplane area and mass distribution about the centerline.

4.3. Viscous drag modeling

Linear wave theory assumes the fluid to be inviscid, incompressible, and irrotational (Faltinsen, 1990). As a consequence, viscous drag is effectively neglected. Viscous drag can have a significant effect on the system response in extreme sea states, i.e., if waves and current effects are much larger than in operational conditions (Zhang et al., 2020; Zheng et al., 2020). Viscous effects are typically included by means of the drag term of Morison's equation. For a slender structural component, the differential viscous load at a given water depth can be expressed as (Zhang et al., 2020):

$$dF_{viscous} = \frac{1}{2}\rho C_d A|u_f - u_c|(u_f - u_c)dl \qquad (5)$$

where $dF_{viscous}$ is the viscous drag acting on a single differential element, C_d is the drag coefficient, A is the projected area per unit length of the component perpendicular to the direction of the flow, u_f is the fluid particle velocity, u_c is the component velocity, and dl is the longitudinal length of the differential element.

Viscous loads have been included in all configurations. In the spar configuration, the viscous load is applied to the main column. In the OO-Star and TLP configurations, the viscous loads are applied to all columns and pontoons. Only transversal viscous drag is assumed to be acting on the pontoons. A drag coefficient equal to 0.65 is used in all configurations.
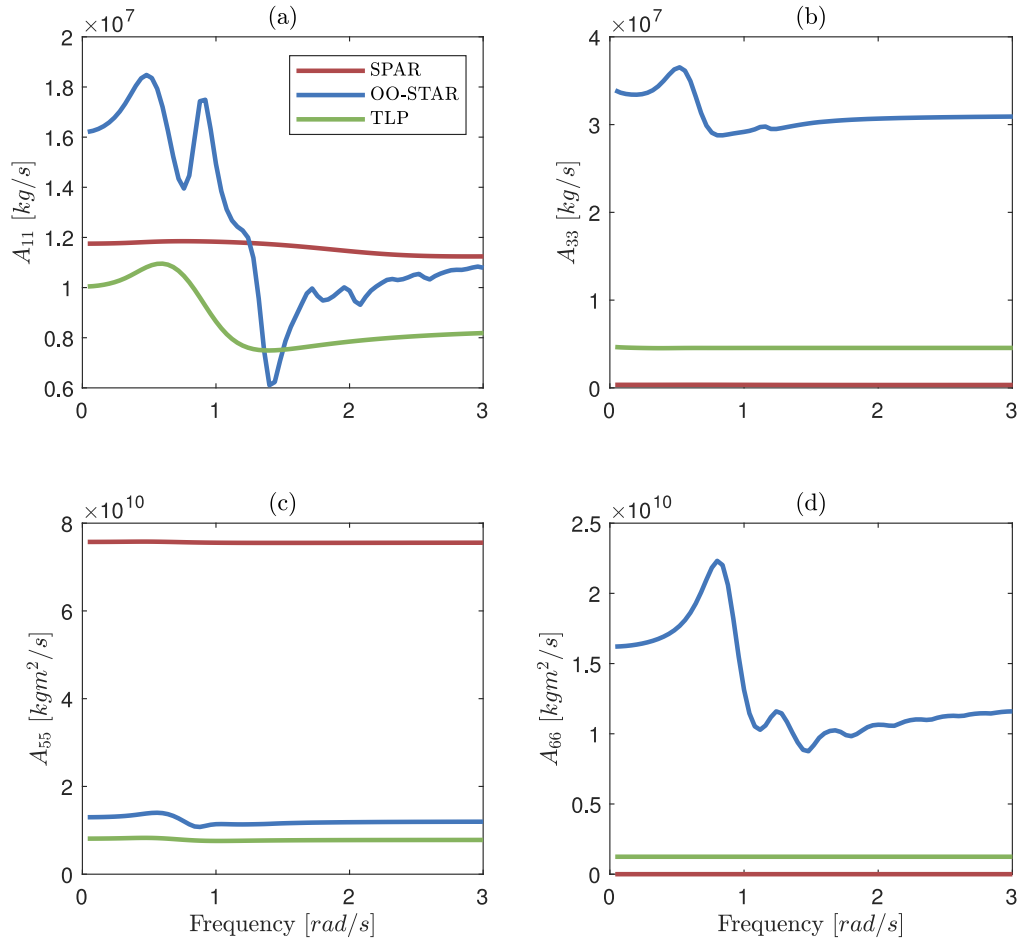
Fig. 4. Major components of the radiative added mass matrix. Platform surge (a), heave (b), pitch (c), and yaw (d) directions.

4.4. Station-keeping

The spar and OO-Star configurations employ catenary mooring lines. The associated station-keeping loads are computed by means of a quasi-static formulation considering the fairleads load–displacement relationship. Additional yaw stiffness is applied to the spar system to account for the delta catenary configuration (about 9.8e7 Nm/rad, as in the Phase IV OC3 design Jonkman, 2010). The TLP configuration employs tendons. The tendon effect on the global system dynamics is approximated by means of a restoring axial stiffness acting between anchor and fairlead. Tendon stiffness is applied to traction loads only, i.e., compression loads are disregarded. Axial stiffness produced by tendons can be computed as:

$$k_t = \frac{E_t A_t}{l_0} \tag{6}$$

where k_t is the tendon axial stiffness, E_t is the tendon Young's modulus, A_t is the tendon cross-sectional area, and l_0 is the tendon unstretched length (Bachynski and Moan, 2012; Du Kim and Jang, 2016). Tendon structural damping is neglected.

4.5. Control system modeling

The baseline NREL control system for the Phase IV OC3 design is employed (Jonkman, 2007, 2010). The control is composed of a rotor-collective blade-pitch proportional-integral (PI) logic on the error between generator speed and the rated generator speed, and it is active at above-rated environmental conditions. The PI-controlled rotor azimuth follows a second-order system dynamics with characteristic natural frequency and damping ratio. These dynamic parameters are often used to properly tune the PI control gains (Jonkman, 2007; Hansen et al., 2005). Recommended natural frequency and damping ratio values for the onshore single-rotor system are 0.6 rad/s and 0.7, respectively. The associated proportional and integral gains at zero blade-pitch angle are 0.0188 and 0.008, respectively. It is well-known how the gains optimized for onshore deployment must be reduced in floating applications to avoid negative damping in the platform pitch direction associated with unfavorable thrust coupling (Jonkman, 2010; Hansen et al., 2005). The PI-controlled rotor dynamics natural frequency must be sufficiently smaller than the natural frequency associated with platform pitch motion to avoid negative damping. As all configurations considered in this work have a platform pitch motion natural frequency higher than that of the reference single-rotor Phase IV OC3 system, the associated reduced gains for offshore application are employed ($K_I = 0.00089$ and $K_P = 0.0062$, associated with a natural frequency and damping ratio of 0.2 rad/s and 0.7, respectively) (Jonkman, 2010). As expected, pitch instability did not occur in the load cases considered in this study. The NREL generator torque control is also employed, aiming at the optimization of aerodynamic power at below-rated environmental conditions and allowing for constant electric power output at above-rated environmental conditions (Jonkman, 2007).

4.6. Load cases

Six load cases are considered in this work, characterized by directionally congruent irregular waves and turbulent wind conditions (Bachynski and Moan, 2012). Table 6 lists the load cases selected.
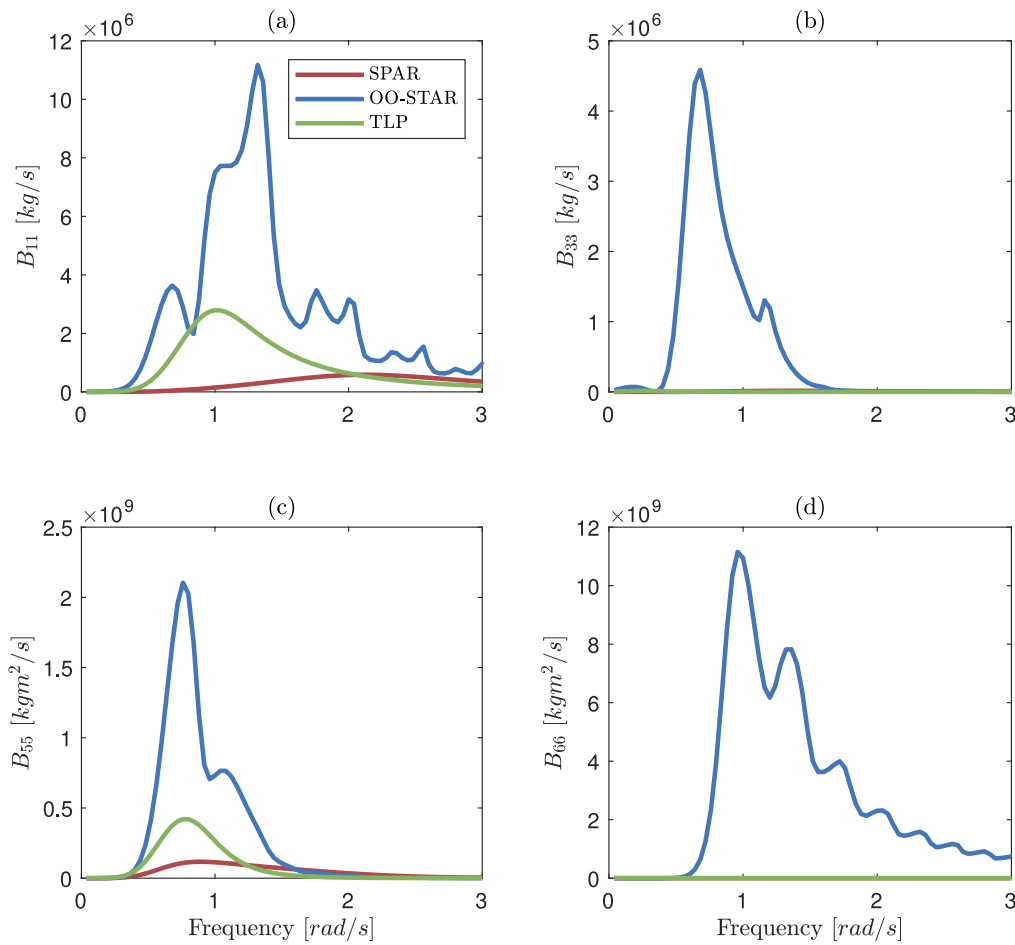
Fig. 5. Major components of the radiative potential damping matrix. Platform surge (a), heave (b), pitch (c), and yaw (d) directions.

Table 6
Load cases (LCs).

		LC1	LC2	LC3	LC4	LC5	LC6
U_W	m/s	8	11.4	14	18	25	50
H_S	m	2.5	3.1	3.6	4.4	5.9	12.7
T_P	s	9.8	10.1	10.2	10.6	11.3	14.1
Simulation time	s	3600	3600	3600	3600	3600	3600
Wind state		NTM/KAI	NTM/KAI	NTM/KAI	NTM/KAI	NTM/KAI	NTM/KAI
Wave spectrum		JSP	JSP	JSP	JSP	JSP	JSP

NTM: normal turbulence model (type B); KAI: Kaimal turbulence; JSP: JONSWAP.

Irregular waves are produced by JONSWAP spectra. LC1 is relative to below-rated environmental conditions, LC2 to the rated environmental condition, and LC 3–5 to above-rated environmental conditions. In LC5 the wind turbine is parked with fully-pitched blades. Finally, LC6 represents an extreme storm condition where the wind turbine is parked with fully-pitched blades. Wave energy content increases in accord with the wind condition. Kaimal wind turbulence model is used, based on the standard IEC 61400-2 (International Electrotechnical Commission, 2005). A normal turbulence model of class B (NTM-B) is used to define the turbulence intensity associated with each LC. The same wind and wave time realizations are applied to all FOWT configurations.

5. Results and discussion

5.1. Natural periods

Table 7 lists the damped natural periods of each configuration obtained through free decay tests in Modelica. Free decay tests are carried

Table 7
Damped natural periods obtained from free decay tests.

		SPAR	OO-STAR	TLP
Surge	s	132.3	147.5	44.3
Heave	s	32.1	18.5	0.65
Pitch	s	29.7	23.8	1.05
Yaw	s	33.6	108.6	25.1

out in still water and without incoming wind. The flexibility of the OO-Star and TLP pontoons and columns may have a significant effect on the natural periods of the system (especially in the platform heave and pitch directions) (Berthelsen, 2015; Bachynski and Moan, 2012). The TLP tendons mass and added mass may also have a significant effect on the natural period in the platform yaw direction (Bachynski and Moan, 2012). The OO-Star natural period in the platform heave direction is short relative to the spar configuration, given the larger waterplane area and the stiffer mooring lines employed. The large yaw inertia of the OO-Star configuration leads to a significantly longer natural period
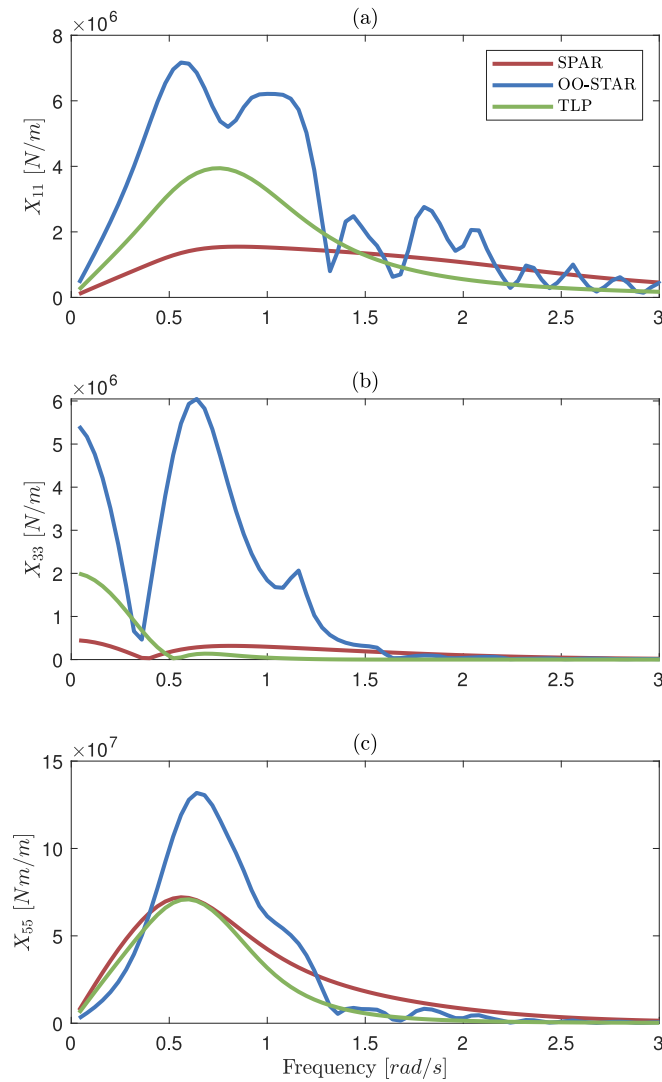
Fig. 6. Major components of the incident wave loading matrix. Platform surge (a), heave (b), and pitch (c) directions.

in the platform yaw direction if compared to the other configurations. TLP natural periods are well within the limits imposed by the design criteria considered (Bachynski and Moan, 2012).

5.2. Dynamic response

Fig. 7 shows the overall mean values of platform surge and pitch motions, electric power output, and nacelle horizontal acceleration for the considered load cases. Results are relative to the left wind turbine only. The mean values of platform surge motion are directly associated with the equivalent stiffness of the mooring system. As a consequence, the spar configuration experiences the highest mean response (about twice the values obtained in the OO-Star system) because it employs the softest station-keeping system. The mean values of platform pitch motion are instead mainly associated with the pitch hydrostatic stiffness and the configuration layout. The platform static pitch angle due to a given thrust can be estimated as (El Beshbichi et al., 2021a):

$$\phi_5 = \frac{F_T H B}{C_{55} + K_{55}} \qquad (7)$$

where ϕ_5 is the platform pitch angle, F_T is the thrust acting on the structure, HB is the vertical distance between hub and CoB, and K_{55} is the stiffness due to the station-keeping system in the platform pitch direction. Although the hydrostatic pitch stiffness is highest for the spar configuration (Table 5), the associated mean platform pitch response

is the highest due to the significant longer distance HB and the low stiffness due to the station-keeping system. The TLP is clearly the best performing configuration, showing negligible mean platform pitch motion and mean platform surge motion well within the offset limit imposed in the design stage (about 3.6 m offset at the rated wind speed). Only the power output relative to the left wind turbine is depicted, as results associated with the right wind turbine are analogous. Electric power output close and above the rated wind speed is lower than the rated value, i.e., 5 MW, due to turbulent fluctuations of the generator speed to below-rated values (El Beshbichi et al., 2021a). The different configurations lead to similar electric power generated throughout the load cases considered. The spar configuration leads to a slight reduction of mean electric power at below-rated wind speeds (about −140 kW difference if compared to OO-Star and TLP at the rated wind speed). This may be associated with a larger global response of the system in the platform pitch and yaw directions, which can reduce the aerodynamic efficiency due to the skewed flow. The nacelle horizontal acceleration is characterized by near-zero mean values. The reduction of aerodynamic loads due to fully-feathered blades leads to overall negligible mean responses in extreme storm conditions.

Fig. 8 shows the platform yaw motion standard deviation (STD) and maximum value (MAX) for the load cases considered. The figure shows clearly how platform yaw motion is significant for all configurations considered. Platform yaw motion is particularly significant in the spar
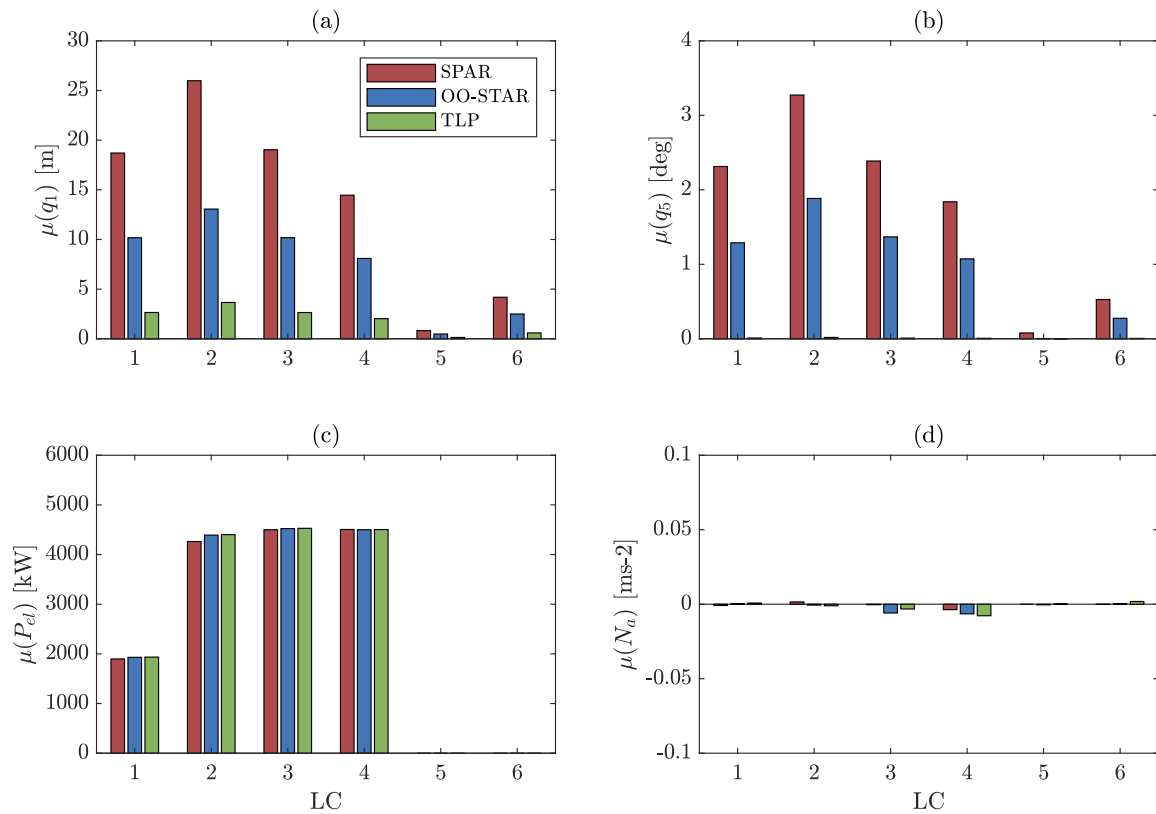
Fig. 7. Mean values of (a) platform surge motion, (b) platform pitch motion, and (c) electric power output, and (d) nacelle horizontal acceleration. Results are relative to the left wind turbine.
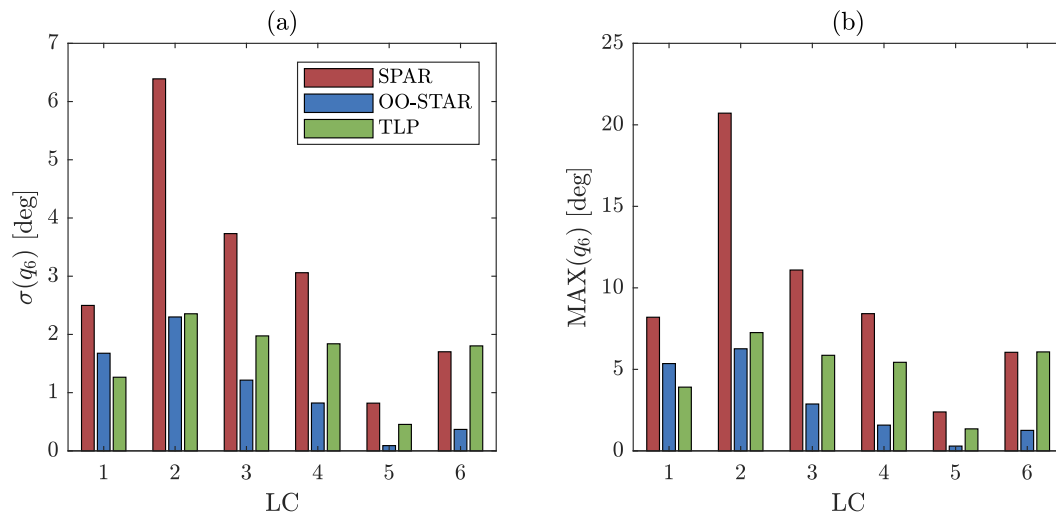

Fig. 8. Platform yaw motion standard deviation and maximum values.

configuration, showing a STD value of about 6.2 deg and MAX of about 20.4 deg at the rated wind speed. These values are in good accordance with results obtained in previous work by means of simplified aerodynamic methods (El Beshbichi et al., 2021a). In the same work, it was shown how platform yaw motion is directly caused by the wind turbulence intensity coupled with the transversal thrust distribution on the tower structure. Although the OO-Star and TLP configurations show a relatively appreciable platform yaw response, their magnitude is significantly lower than in the spar configuration. This can be directly associated with stiffer station-keeping systems and a markedly longer fairlead distance to the platform centerline, increasing the effective platform yaw stiffness (Faltinsen, 1990).

Fig. 9 shows the overall STD values of platform surge and pitch motions, electric power output, and nacelle horizontal acceleration for the load cases considered. Whilst mean values are in the main associated with the mean wind speed, STD values are also affected by wind turbulence intensity and the hydrodynamic loadings acting on the floating platform (e.g., see the response in parked and extreme storm conditions). Within operational environmental conditions, the highest platform surge STD is obtained for the spar configuration at the rated environmental condition. Platform surge STD presents a similar trend with respect to its mean value. Moreover, platform surge STD is greatly increased in extreme storm conditions, with peak values obtained for the OO-Star configuration of about 4.5 m. Platform pitch STD is highest
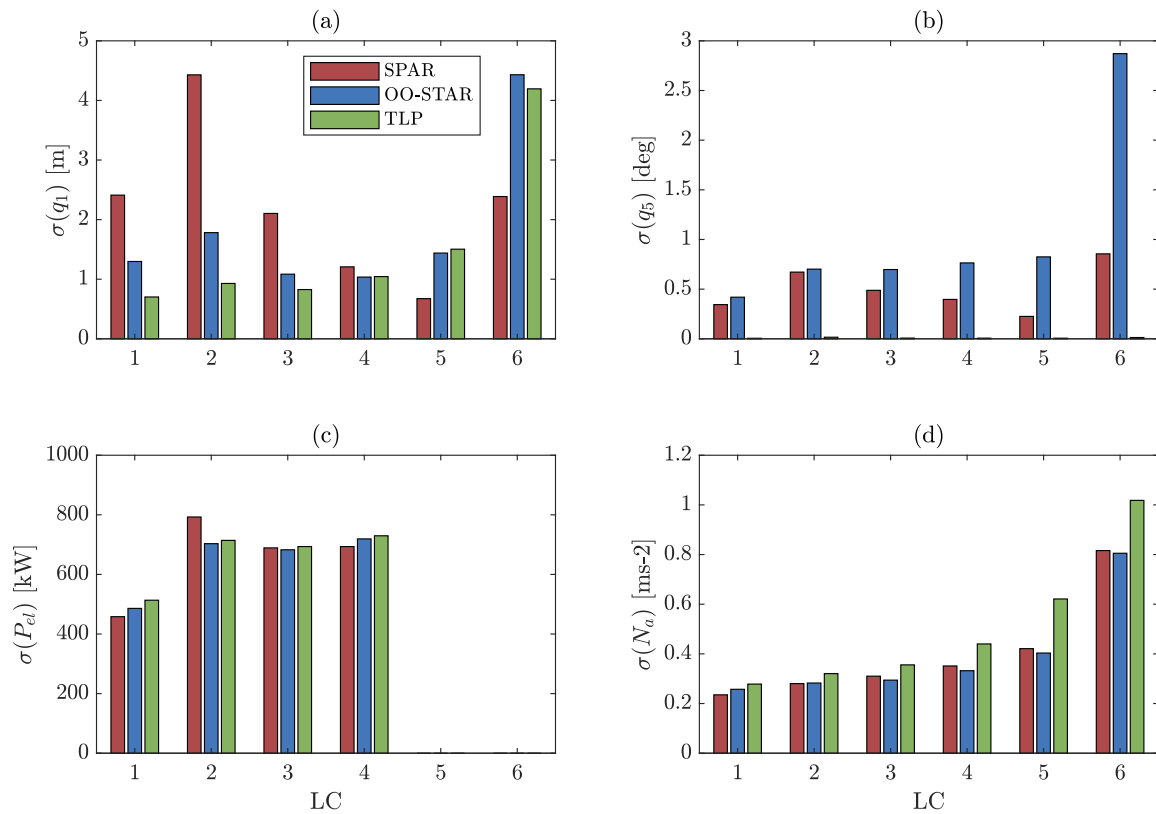
Fig. 9. Standard deviation values of (a) platform surge motion, (b) platform pitch motion, (c) electric power output, and (d) nacelle horizontal acceleration. Results are relative to the left wind turbine.

for the OO-Star configuration, and tends to increase with the severity of the sea state. This can be related to the significant increase in hydrodynamic loading at higher wind speeds, which compensate for the reduction of thrust-induced pitch torque and the reduction of the wind turbulence intensity. On the other hand, platform pitch STD for the spar configuration is reduced at above-rated wind speeds (excluding extreme storm conditions) because the increase of hydrodynamic loading is not sufficient to compensate for the reduction of thrust-induced pitch torque. Platform pitch STD is significantly higher for the OO-Star configuration in the extreme storm load case — about 2.5 times higher than in the spar configuration. A marginally higher electric power output STD for the spar configuration (about 100 kW at the rated wind speed) is a direct consequence of thrust fluctuations given by the large platform yaw and pitch responses, as discussed for Fig. 9. The nacelle horizontal acceleration STD is significantly increased by increased severity of the sea state, with maximum values in the extreme storm condition of about 0.9 m/s². Moreover, results show similar acceleration values among the configurations considered.

Fig. 10 shows the maxima of the performance parameters for the load cases considered. The trend depicted is in accordance with the considerations made for the mean values (especially in the case of the platform surge motion) and STD values (especially for the platform pitch motion). The highest value of the maximum platform pitch motion in the extreme storm condition is about 11 deg for the OO-Star configuration, while the maximum nacelle horizontal acceleration is about 3.5 m/s² and is obtained for the TLP configuration. It is important to remark that the system response is greatly influenced by the blade-pitch control strategy employed, as previous work demonstrated (El Beshbichi et al., 2021a). As a result, designing a specific control logic, such as integrating platform yaw motion as a control target to be minimized, can lead to improved system performance.

5.3. Tower base bending moment

Fig. 11 shows the tower base bending moment mean values, STDs, and maxima for the load cases considered. Values associated with the 2WT employed onshore are also included in the figure (considering 77.6 m tower). A similar trend of the mean values to the one already discussed can be observed, showing the highest mean values in the case of the spar configuration and the lowest in the case of the TLP configuration. Mean tower base bending moment is associated with the magnitude of the external aerodynamic loading and the gravitational loading of the upper structure acting on the main tower. The latter assumes significant values with increasing platform pitch angles. The mean tower base bending moment for the TLP configuration is very similar to the value associated with the tower-fixed deployment, clearly due to the high pitch stiffness. The TLP mean tower base bending moment is also about 65% of the value associated with the spar configuration, and it holds constant for all the load cases considered. This is clearly due to the linear relationship between external loading and associated platform pitch angle, and the relatively small mean platform pitch angles involved (so that $sin\phi_5 \approx \phi_5$).

The tower base bending moments STD tend to increase with the severity of the environmental condition, mainly due to higher hydrodynamic loadings. The tower base bending moment STD for the tower-fixed configuration gives an indication of the relative significance of wind turbulence intensity, contributing to about 30%–40% of the load variability at the rated wind speed.

Fig. 12 shows the tower base bending moment power spectral density (PSD) computed at the rated wind speed (LC2). Wave loading energy is clearly visible around the characteristic wave period (10.1 s– 0.09 Hz) and is similarly distributed for the configurations considered. Turbulent wind energy is also similarly distributed in the low-frequency region.

An increase in the bending moment power density is associated with the excitation given by the platform rigid motion in the pitch and
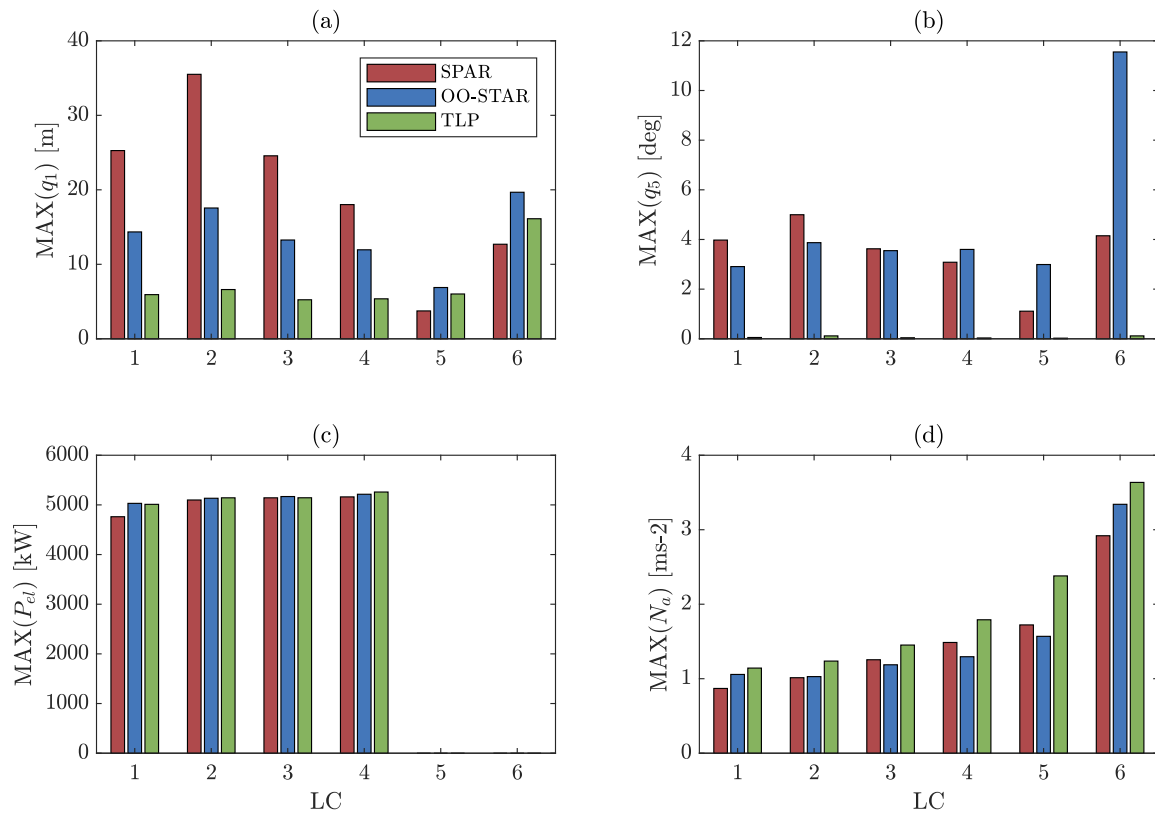
Fig. 10. Maxima of (a) platform surge motion, (b) platform pitch motion, (c) electric power output, and (d) nacelle horizontal acceleration. Results are relative to the left wind turbine.

heave directions, as clearly visible in the peaks at 1 and 1.5 Hz ca. for the TLP configuration and the peaks in the region 0.3–0.5 Hz for the spar and OO-Star configurations. For the TLP configuration, it is known that viscous drag loads acting on the platform can induce springing and increase pitch and heave motions (Shen et al., 2016). The high-frequency energy of the tower base bending moment may contribute to wind turbine component fatigue. Moreover, platform pitch motion may experience coupling effects with elastic modes of the structure. These effects are not considered to date and should be investigated in future work.

5.4. Upstream line tension

The standard deviation of line tension should be sufficiently small to avoid slack conditions and increase fatigue life, and considerations are often made in terms of the ratio between the STD and the mean value (Bachynski and Moan, 2012; Cheng et al., 2017). Fig. 13a shows the ratio between line tension STD and the associated mean value. The largest ratio is obtained for the TLP configuration. It is clear from the figure that STD values are relatively significant if compared to the associated mean tension value (maximum 22% of the mean value for TLP configuration at 11.4 m/s). For the TLP configuration, tendon loads are greatly increased by viscous drag effects (Shen et al., 2016). Maximum line loads reach 60% of the associated mean value for the TLP configuration throughout the load cases considered and for the OO-Star configuration in the extreme storm condition. Large extreme line loads can pose limit state concerns. Fig. 14 shows the upstream lines tension PSD computed at the rated wind speed (LC2). The energy content is clearly different for each configuration given the variation in line pre-tension. The energy content for the TLP configuration, for instance, is about four orders of magnitude higher than in the spar configuration at the wave frequency. In the TLP configuration, peaks are clearly visible at the platform heave and pitch natural frequencies.

6. Conclusions

This work presented a comparative dynamic performance analysis of a two-rotor wind turbine mounted on three different floating platforms, i.e., a spar-type, a semi-submersible, and a tension-leg. The system employed 5-MW baseline wind turbines from NREL. The spar-type and tension-leg platform designs have been defined by means of simplified hydrostatic considerations applied to the two-rotor system. The well-known OO-Star platform design, originally defined for the DTU 10-MW baseline wind turbine, is instead considered as a reference semi-submersible platform. The OO-Star ballast mass is adjusted to compensate for the different overall system mass when employed with the two-rotor system to keep the original draft and water displacement. Fully-coupled dynamic simulations are performed by means of an in-house code developed in Modelica. The tool implements state-of-the-art simulation capabilities and integrates the well-established blade-element momentum code AeroDyn v15 from NREL to compute aerodynamic loads. Six load cases are used to assess the dynamic response of the concepts considered, composed of directionally congruent turbulent wind and irregular wave profiles.

Results indicate that platform yaw motion is a significant dynamic mode for each configuration. This result is in accordance with previous work employing simplified aerodynamics. The greatest yaw response is obtained for the spar configuration. Yaw motion can be directly correlated with the equivalent yaw stiffness of the system, which can be related to the stiffness of the station-keeping lines and the fairlead distance to the platform centerline. The spar configuration employs the softest mooring lines and the shortest fairlead radius, thus resulting in amplified yaw response. Yaw response is shown to negatively contribute to the rotors' electric power output quality by increasing the associated standard deviation (about +100 kW if compared to TLP configuration). It is important to remark that the system response is greatly dependent on the blade-pitch control logic employed, as
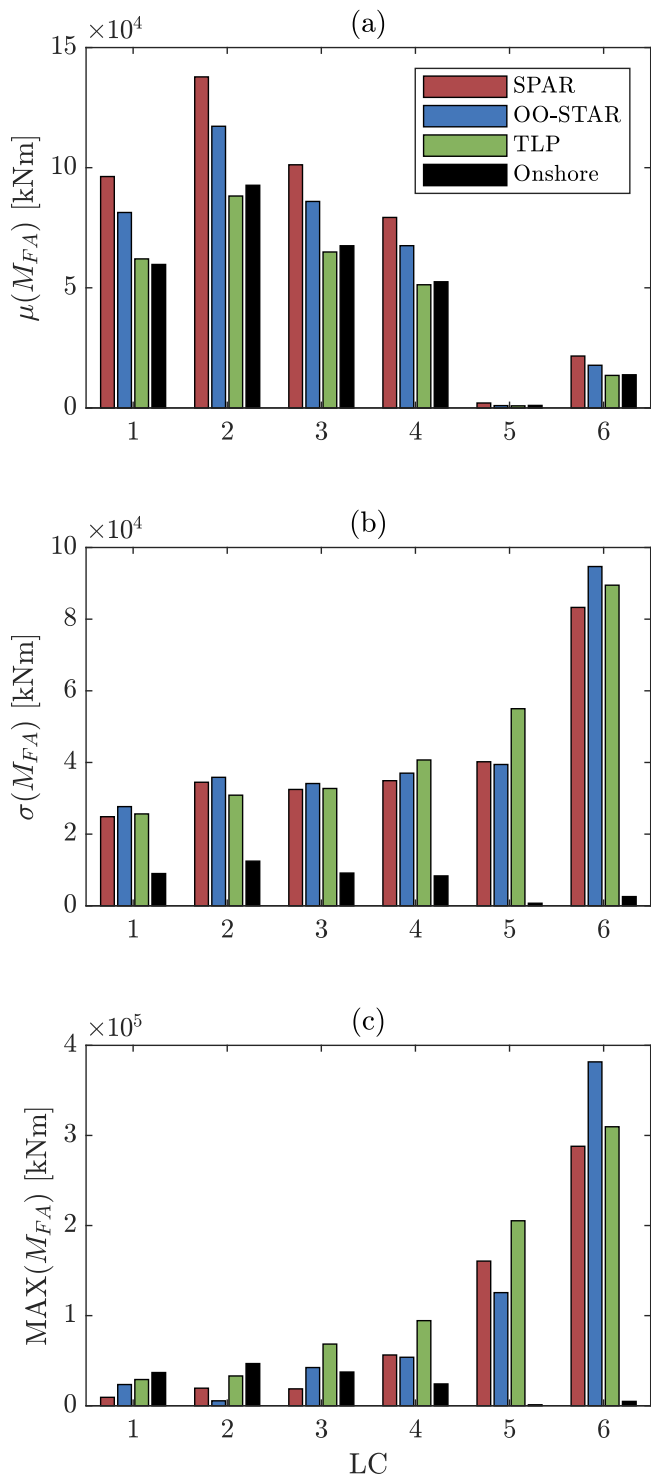
Fig. 12. Tower base bending moment PSD (LC2 - U_W = 11.4 m/s, H_S = 3.1 m, T_P = 10.1 s). Tower and blades are assumed rigid.

Fig. 11. Tower base bending moment (a) mean value, (b) standard deviation, and (c) maximum value. Onshore tower base bending moment is also included (77.6 m tower).

previous work on the subject demonstrated. The inclusion of platform yaw response mitigation as additional control objective can greatly improve the system response.

The mean response of the performance parameters is largely associated with wind loading. Mean platform pitch motion is greatest for the spar configuration, given the largest distance between thrust loads and center of buoyancy. Skewed conditions given by mean pitch motion can contribute to the reduction of the mean electric power output. The
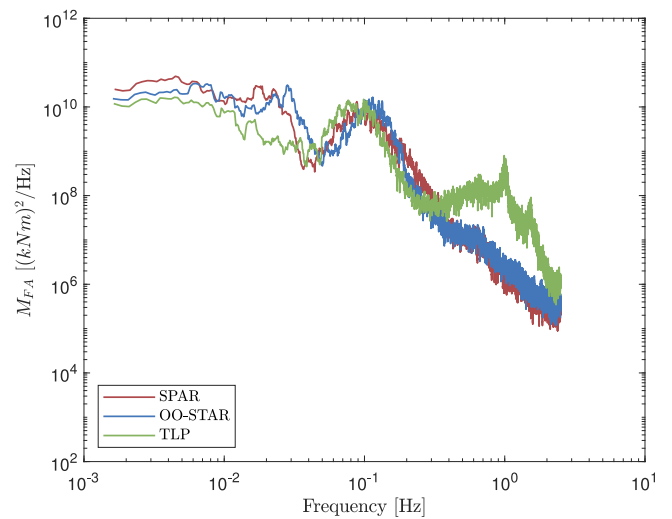
mean tower base bending moment obtained for the spar configuration is largest due to weight loads induced by the large mean platform pitch angle.

The tower base bending moment standard deviation is clearly much greater than in the case of the equivalent system deployed onshore. The dynamic variation is mainly associated with the hydrodynamic loads acting on the platform, as clearly visible in the fully-pitched load case (LC5). The periodic variation of tower base bending moment can lead to significant fatigue damage. The associated STD increases with increased sea state severity, and it is especially high in extreme storm conditions. Tower base bending moment power spectral density also showed significant energy content at the platform heave and pitch natural frequencies (about 1.5 and 1 Hz, respectively) for the TLP configuration. This high-frequency load variation may have a significant impact on tower fatigue life. Moreover, line tensions standard deviations and maxima normalized by the associated mean value are highest for the TLP configuration, reaching 22% and 60%, respectively. These high values may pose concerns regarding fatigue and limit state performance of the tendons.

Even though a candidate floating platform design is still to be selected, it is clear that the spar configuration is not ideal for multi-rotor applications given the excessive platform yaw amplification and large mean pitch angle which reduce the aerodynamic efficiency of the rotors. The TLP configuration rigidity entails improved dynamic response but may lead to excessive structural loading on the system components and fatigue damage of tower, blades, and tendons, especially for intense sea states. The semi-submersible configuration, even though associated with a platform design not optimized for the specific application and associated with large responses in extreme storm conditions, tended to the most balanced response in operational conditions. Results can be greatly improved by the utilization of a blade-pitch control strategy specifically designed for the multi-rotor system. The present work is limited in scope, given the assumptions employed, the limited amount of load cases considered, and the short-term nature of the time realizations. The results presented may be nonetheless used as a basis for further detailed dynamic analysis.

Several assumptions have been used in this work. First, complex aerodynamic effects such as the aerodynamic interaction between the rotors are neglected. These effects may have important dynamic consequences and should later be investigated with higher fidelity tools. In the next future, a dedicated correction factor will be included in the code. Aerodynamic drag on the tower is not considered, as well as the aerodynamic effect of the tower on the local wind profile. Moreover,
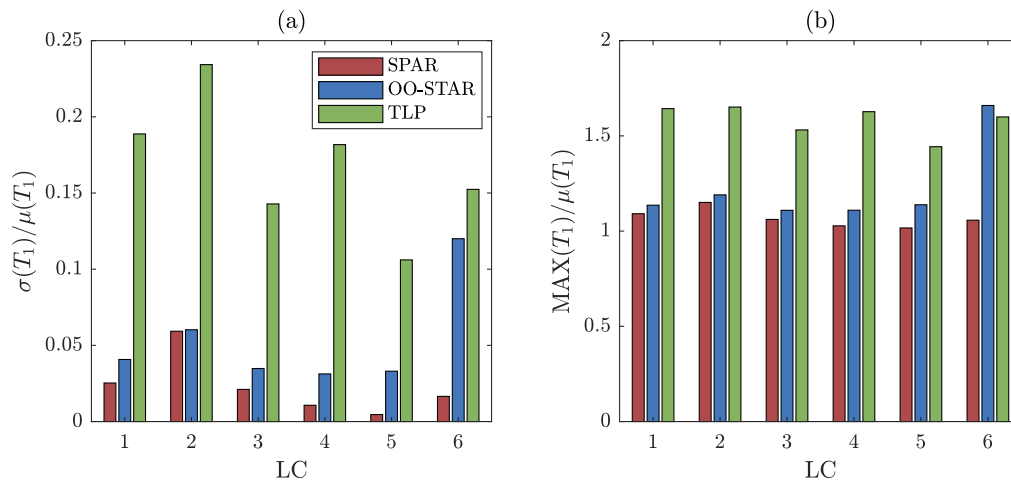
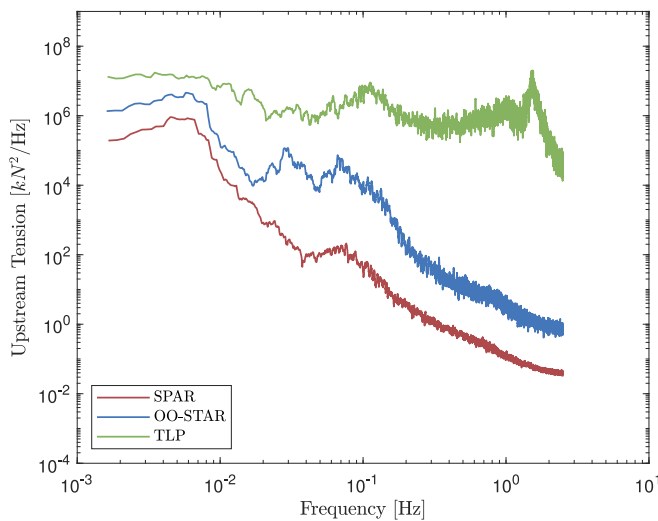**Fig. 13.** Line tensions. (a) Ratio between STD and mean values. (b) Ratio between maximum and mean value.

Fig. 14. Upstream line tension PSD (LC2 - U_W = 11.4 m/s, H_S = 3.1 m, T_P = 10.1 s). Tower and blades are assumed rigid.

tower and blades have been assumed rigid. Aeroelastic effects are thus not visible in the present results. The analysis of the aforementioned issues will be covered in future work. Moreover, the present work can be further expanded by performing a comparative dynamic analysis of the two-rotor wind turbine against a single-rotor wind turbine with the same installed power capacity.

CRediT authorship contribution statement

Omar El Beshbichi: Conceptualization, Methodology, Software, Validation, Formal analysis, Investigation, Writing – original draft, Writing – review & editing, Visualization. **Yihan Xing:** Conceptualization, Methodology, Software, Formal analysis, Investigation, Writing – review & editing, Supervision. **Muk Chen Ong:** Conceptualization, Investigation, Writing – review & editing, Resources, Supervision, Project administration, Funding acquisition.

Declaration of competing interest

The authors declare that they have no known competing financial interests or personal relationships that could have appeared to influence the work reported in this paper.

Data availability

Data will be made available on request.

References

Aerodyn Engineering, 2021. Official Website (Accessed: September 2022). https://aerodyn-engineering.com/products/nezzy-technology/.

Alvarez, E., Ning, A., 2019. Modeling multirotor aerodynamic interactions through the vortex particle method. AIAA 2019-2827. http://dx.doi.org/10.2514/6.2019-2827.

Bachynski, E.E., Moan, T., 2012. Design considerations for tension leg platform wind turbines. Mar. Struct. 29 (1), 89–114. http://dx.doi.org/10.1016/j.marstruc.2012.09.001.

Bak, C., Zahle, F., Bitsche, R., Kim, T., Tde, A., Henriksen, L.C., Hansen, M.H., Blasques, J.P.A.A., Gaunaa, M., Natarajan, A., 2013. The DTU 10-MW Reference Wind Turbine.

Bastankhah, M., Abkar, M., 2019. Multirotor wind turbine wakes. Phys. Fluids 31, 085106. http://dx.doi.org/10.1063/1.5097285.

Berthelsen, A.P., 2015. Qualification of innovative floating substructures for 10 MW wind turbines and water depths greater than 50 m.

Cheng, Z., Madsen, H.A., Gao, Z., Moan, T., 2017. Effect of the number of blades on the dynamics of floating straight-bladed vertical axis wind turbines. Renew. Energy 101, 1285–1298. http://dx.doi.org/10.1016/j.renene.2016.09.074.

Cruz, J., Atcheson, M., 2016. Floating Offshore Wind Energy. The Next Generation of Wind Energy. Springer, http://dx.doi.org/10.1007/978-3-319-29398-1.

Cummins, W.E., 1962. The impulse response function and ship motions (accessed: September 2022). In: Report (David W. Taylor Model Basin), United States Department of the Navy, David Taylor Model Basin, https://hdl.handle.net/1721.3/49049.

DNV, 2021. WADAM - Frequency domain hydrodynamic analysis of stationary vessels.

Du Kim, J., Jang, B.S., 2016. Application of multi-objective optimization for TLP considering hull-form and tendon system. Ocean Eng. 116, 142–156. http://dx.doi.org/10.1016/j.oceaneng.2016.02.033.

El Beshbichi, O., Xing, Y., Ong, M.C., 2021a. Dynamic analysis of two-rotor wind turbine on spar-type floating platform. Ocean Eng. 236, 109441. http://dx.doi.org/10.1016/j.oceaneng.2021.109441.

El Beshbichi, O., Xing, Y., Ong, M.C., 2021b. An object-oriented method for fully coupled analysis of floating offshore wind turbines through mapping of aerodynamic coefficients. Mar. Struct. 78, 102979. http://dx.doi.org/10.1016/j.marstruc.2021.102979.

EnBW, 2021a. Floating wind turbine: Nezzy2 - Website (Accessed: September 2022). https://www.enbw.com/renewable-energy/wind-energy/our-offshore-wind-farms/nezzy2-floating-wind-turbine/.

EnBW, 2021b. Official Website (Accessed: September 2022). https://www.enbw.com/company/.

Equinor, 2022. Hywind Scotland Pilot Park. Environmental Statement, Non Technical Summary. (Accessed: September 2022). https://marine.gov.scot/sites/default/files/hywind.pdf.

Faltinsen, O., 1990. Sea loads on ships and offshore structures. https://osti.gov/biblio/5464335.

Flex2Power, 2022. Official Website (Accessed: September 2022). https://flex2power.com/.

Global Wind Energy Council, 2022. Global Wind Report 2021. (Accessed: September 2022). https://gwec.net/market-intelligence/resources/.

Hansen, M.H., Hansen, A.D., Larsen, T.J., Øye, S., Sørensen, P., Fuglsang, P., 2005. Control design for a pitch-regulated, variable speed wind turbine. Denmark. Forskningscenter Risoe. Risoe-R, (1500(EN)).

Hexicon, 2021a. Operations Update Q2 2021 (Accessed: September 2022). https://www.hexicongroup.com/app/uploads/2022/06/Hexicon-operations-update-18-Aug-2021-final.pdf.

Hexicon, 2021b. Press release - Hexicon to develop TwinWay project for floating wind in Norway (Accessed: September 2022). https://storage.mfn.se/93f0731e-d179-4592-bb2d-30302d2faafb/hexicon-to-develop-twinway-project-for-floating-wind-in-norway.pdf.

International Electrotechnical Commission, 2005. Wind turbines: part 1: design requirements. Tech. rep. IEC61400-1:2005(e).

Jamieson, P., Branney, M., 2012. Multi-rotors; A solution to 20 MW and beyond? Energy Procedia 24, 52–59. http://dx.doi.org/10.1016/j.egypro.2012.06.086.

Jonkman, J., 2007. Dynamics Modeling and Loads Analysis of an Offshore Floating Wind Turbine. http://dx.doi.org/10.2172/921803.

Jonkman, B.J., 2009. TurbSim user's guide: version 1.50. http://dx.doi.org/10.2172/965520.

Jonkman, J., 2010. Definition of the Floating System for Phase IV of OC3. http://dx.doi.org/10.2172/979456.

Jonkman, J., Buhl, B., 2005. FAST User's Guide. http://dx.doi.org/10.2172/15020796.

van der Laan, M.P., Andersen, S.J., Ramos García, N., Angelou, N., Pirrung, G.R., Ott, S., Sjöholm, M., Sørensen, K.H., Vianna Neto, J.X., Kelly, M., Mikkelsen, T.K., Larsen, G.C., 2019. Power curve and wake analyses of the vestas multi-rotor demonstrator. 4, pp. 251–271. http://dx.doi.org/10.5194/wes-4-251-2019,

LIFES50+, 2022. Official Website (Accessed: September 2022). https://lifes50plus.eu/.

Moriarty, P.J., Hansen, A.C., 2005. AeroDyn Theory Manual. http://dx.doi.org/10.2172/15014831.

OSMC, 2021. OpenModelica User's Guide. Release v1.19.0.

Pegalajar-Jurado, A., Bredmose, H., Borg, M., Straume, G.J., Landb/o, T., Andersen, S.H., Yu, W., Müller, K., Lemmer, F., 2018. State-of-the-art model for the LIFES50+ OO-star wind floater semi 10 MW floating wind turbine. J. Phys. Conf. Ser. 1104, 012024. http://dx.doi.org/10.1088/1742-6596/1104/1/012024.

Principle Power, 2022. The WindFloat: Enabling a Paradigm Shift in Offshore Wind. (Accessed: September 2022). https://ngi.no/download/file/5505.

Shen, M., Hu, Z., Liu, G., 2016. Dynamic response and viscous effect analysis of a TLP-type floating wind turbine using a coupled aero-hydro-mooring dynamic code. Renew. Energy 99, 800–812. http://dx.doi.org/10.1016/j.renene.2016.07.058.

The Modelica Association, 2008. Modelica Standard Library. Tutorial and Reference. Version 3.0.

The Modelica Association, 2017. Modelica® - A Unified Object-Oriented Language for Systems Modeling. Language Specification, Version 3.4.

Wind Catching Systems, 2022. Official website (accessed: September 2022). https://windcatching.com/.

Zhang, L., Shi, W., Karimirad, M., Michailides, C., Jiang, Z., 2020. Second-order hydrodynamic effects on the response of three semisubmersible floating offshore wind turbines. Ocean Eng. 207, 107371. http://dx.doi.org/10.1016/j.oceaneng.2020.107371.

Zheng, Z., Chen, J., Liang, H., Zhao, Y., Shao, Y., 2020. Hydrodynamic responses of a 6 MW spar-type floating offshore wind turbine in regular waves and uniform current. Fluids 5 (4), http://dx.doi.org/10.3390/fluids5040187.

Zhou, W., Ning, Z., Li, H., Hu, H., 2017. An experimental investigation on rotor to rotor interactions of small UAV. AIAA 2017-3744. http://dx.doi.org/10.2514/6.2017-3744.